International Journal of Fatigue 97 (2017) 190–201

Contents lists available at ScienceDirect

International Journal of Fatigue

journal homepage: www.elsevier.com/locate/ijfatigue

The effects of inhomogeneous microstructure and loading waveform on creep-fatigue behaviour in a forged and precipitation hardened nickel-based superalloy

Run-Zi Wang [a], Bo-Chen [b], Xian-Cheng Zhang [a,*], Shan-Tung Tu [a,*], Ji-Wang [a], Cheng-Cheng Zhang [c]

[a] Key Laboratory of Pressure Systems and Safety, Ministry of Education, East China University of Science and Technology, Shanghai 200237, PR China
[b] The Institute for Advanced Manufacturing and Engineering, Faculty of Engineering, Environment and Computing, Coventry University, Coventry CV6 5LZ, UK
[c] AECC Commercial Aircraft Engine Co. LTD, Shanghai Engineering Research Center for Commercial Aircraft Engine, Shanghai 201108, PR China

ARTICLE INFO

Article history:
Received 10 October 2016
Received in revised form 29 December 2016
Accepted 2 January 2017

Keywords:
Creep-fatigue
Nickel-based superalloy
Microstructure
Failure mechanism
Oxidation

ABSTRACT

The aim of the present paper is to identify the effects of sampling locations and loading waveforms on high-temperature low-cycle fatigue (HTLCF) and creep-fatigue life of a forged and precipitation hardened nickel-based GH4169 superalloy. Both the deformation and failure mechanisms are considered here. It has been revealed that HTLCF and creep-fatigue life of specimens were influenced by inhomogeneous microstructures at different locations. Compared with the HTLCF tests, the presence of dwell times in creep-fatigue tests tended to reduce number of cycles to failure. Intergranular damage was observed at both crack initiation and propagation stages. For the dwell times under tension, the intergranular damage was mainly associated with precipitate-assist voids. However, oxidation accounted for the presence of intergranular damage for the dwell times under compression.

© 2017 Published by Elsevier Ltd.

1. Introduction

The nickel-based superalloy GH4169 has been found to exhibit good mechanical properties and corrosion resistance, excellent weld ability as well as long-term thermal stability [1]. Both the microstructures and mechanical properties of GH4169 are similar to those of Inconel 718 [1,2]. These two types of superalloys are widely used for rotating components such as discs and spacers of gas turbine engines [1,3]. Such components operate at high temperatures ranging from 300 °C up to 650 °C where fatigue, creep and oxidation processes limit their service lifetimes [3–5]. Depending on the specific service condition of the component, the failure mode may change drastically from transgranular to intergranular due to the cumulative effects of microstructures, creep and oxidation [3,6,7]. Previous studies [4,6,8–12] showed that the presence of creep dwells in creep-fatigue tests led to a reduced number of cycles to failure when compared with that of pure fatigue tests. In addition, oxidation effects need to be considered when interpreting some creep-fatigue test data, in particular for certain loading waveforms [7,13,14].

Material properties required to carry out the high temperature structural integrity assessment are derived from high-temperature low-cycle fatigue (HTLCF) and creep-fatigue tests [15]. The dwell periods of creep-fatigue tests under strain-controlled conditions are usually introduced at either the maximum tensile or compressive strain or both of them. Both the HTLCF and creep-fatigue lifetimes depend not only on temperatures but also on loading waveforms [8]. Brinkman et al. [16,17] reported that both the HTLCF and creep-fatigue lifetimes decreased with the increasing temperatures for Inconel 718 and several high temperature structural materials. Wei and Yang [4] carried out both the HTLCF and creep-fatigue tests on cast GH4169 superalloy at a temperature of 650 °C. It was found that the presence of dwell periods in creep-fatigue tests caused a reduction of up to 50% in fatigue lifetime and the reduced magnitudes varied with the total strain ranges. Typical loading waveform variables in a fully reversed test ($R_\varepsilon = -1$) are the total strain range, $\Delta\varepsilon_t$, the dwell time at the maximum tensile strain, t_d, and that at the maximum compressive strain, t_e. It has been found that the effect of creep dwells on fatigue lifetimes of high-temperature structural materials including GH4169 [4], Inconel 718 [16,17], M963 nickel-based superalloys [18], modified 9Cr-1Mo steel [17], 304 and 316 stainless steels [17], depended on those three loading waveform variables.

* Corresponding authors at: Key Laboratory of Pressure Systems and Safety, Ministry of Education, School of Mechanical and Power Engineering, East China University of Science and Technology, Meilong Road 130, Xuhui District, Shanghai 200237, PR China.

E-mail addresses: xczhang@ecust.edu.cn (X.-C. Zhang), sttu@ecust.edu.cn (S.-T. Tu).

http://dx.doi.org/10.1016/j.ijfatigue.2017.01.002
0142-1123/© 2017 Published by Elsevier Ltd.

Both the HTLCF and creep-fatigue behaviours of nickel-based superalloys could be affected by their microstructures [3,19,20]. Prasad et al. [19] carried out both the HTLCF and creep-fatigue tests at 650 °C on a forged disc of Inconel 718. Test specimens were extracted from three locations namely, rim, hub and bore regions of the disc. The bore accumulated less intergranular damage per cycle and thus had a higher number of cycles to failure when compared with those for the hub and rim [19]. This seems to be related with the different grain size and grain structure for the bore. Prasad et al. [19] reported that the average grain size for both the rim and hub was ~20 μm, but an intermixed grain structure was found for the bore with the grain size of ~10 μm for the finer grains and ~25 μm for the coarser grains. In addition, Khajaet al. [20] observed that room temperature tensile and cyclic behaviours of the forged and precipitation hardened Inconel 718 disc varied with the sampling location due to microstructural inhomogeneity. However, it is still not clear whether the HTLCF and creep-fatigue behaviours of the forged and precipitation hardened nickel-based superalloy are also sampling location dependent.

In the present paper, we report an experimental study of the effects of inhomogeneous microstructure and loading waveform on the HTLCF and creep-fatigue behaviours of a forged and precipitation hardened GH4169 superalloy at 650 °C. Measurements of grain size, micro-hardness, the numbers of intergranular δ phase and Σ3 coincident site lattice (CSL) boundaries were carried out on the specimens that had been extracted from different locations of the GH4169 disc. Various combinations of $\Delta\varepsilon_t$, t_d and t_e were selected to study the effect of the loading waveform. Finally, the deformation and damage mechanisms of GH4169 superalloy under HTLCF and creep-fatigue conditions were discussed with respect to the microstructure and fractography examinations.

2. Experimental

2.1. Material and heat treatment

The GH4169 superalloy, removed from a radial forging formed disc with a diameter of 180 mm, was provided by Fushun Special Steel Co., Ltd. The disc was manufactured by the following procedures: dual smelting, high temperature diffusion annealing, cogging, and then finished with radial forging process. Dual smelting included vacuum induction and the following vacuum self-consuming arc melting. High temperature diffusion annealing included following stages: first heating at 1160 °C for 24 h, second heating at 1190 °C for 72 h, and finally air cooling to room temperature. After ingoting scalping and confirming flawless surface, the final forging process was carried out by a hydraulic radial forging machine. Cylindrical bars with a diameter of 14 mm and a length of 100 mm were extracted by EDM wire-cut machine from three pre-defined locations of the forged disc: (a) outermost, (b) middle, and (c) innermost, as schematically shown in Fig. 1a. All three groups of cylindrical bars were then subjected to the same heat treatment that included the following steps: solid solution at 960 °C for 1 h, air cooling, first-stage aging at 720 °C for 8 h, cooling at 50 °C /h to 620 °C, second-stage aging at 620 °C for 8 h, and finally air cooling to the room temperature. This heat treatment procedure was selected to obtain the optimised precipitation hardened microstructure and the heat treatment parameters can be considered as the common industrial practice for GH4169 superalloy [21]. A similar heat treatment procedure had been applied previously to Inconel 718 superalloys to improve their creep-fatigue performance of [16,20,22]. The nominal chemical composition of GH4169 superalloy is given in Table 1, which is similar to that of Inconel 718 [16,20,22].

2.2. HTLCF and creep-fatigue testing

Uniaxial round bar test specimens with a gauge length of 8 mm and a gauge diameter of 6 mm were machined out of the heat treated cylindrical bars. Detailed dimensions of the test specimens are shown in Fig. 2. Finally, the gauge portion of each specimen was polished down to 1 μm diamond. Both the HTLCF and creep-fatigue tests were carried out on an Instron 8500 servo-hydraulic machine by using strain-controlled triangular and trapezoidal loading waveforms. All tests were conducted at a temperature of 650 °C ± 2 °C in air environment under fully reversed loading condition ($R_\varepsilon = -1$) with a constant strain rate of 0.4%/s. A high temperature extensometer, attached to the gauge-length area of the specimen, was used to monitor the axial strain during the strain-controlled tests. The end-of-test was defined to be the 40% decrease in the cyclic maximum tensile stress, conforming to ASTM E-2714-13 standard [23].

Table 2 summarises test parameters for each specimen and the characteristic locations of the disc where each specimen was extracted. Specimens F-1 to F-10 were subjected to HTLCF tests with $\Delta\varepsilon_t$ ranging from 1.0% to 2.0%, Table 2. Specimens F-1 to F-4 were extracted from the outermost location of the disc, specimens F-5 to F-8 were from the middle location, and specimens F-9 and F-10 were from the innermost location of the disc, Table 2. They were used to investigate the effects of both the total strain range and sampling location on high temperature low cycle fatigue (HTLCF) behaviour. Specimens CF-1 to CF-8 were extracted from the outermost location of the disc and then tested under creep-fatigue conditions, Table 2. These specimens were compared with pure fatigue loading specimens F-1 to F-4 to study the effects of creep dwells. Within this group, specimens CF-1, CF-3, CF-5 and CF-7 were tested with creep dwells at the maximum tensile strain ($t_d = 300$ s) and specimens CF-2, CF-4, CF-6 and CF-8 were tested with creep dwells at the maximum compressive strain ($t_e = 300$ s). Specimens CF-7 to CF-12 were creep-fatigue tested with $\Delta\varepsilon_t = 2.0\%$, Table 2, and they were used to examine the effect of sampling location on creep-fatigue behaviour of GH4169 superalloy. The following abbreviations are used throughout the paper: (i) 0–0 stands for HTLCF test without creep dwells, (ii) 300–0 stands for creep-fatigue test with the creep dwells applied at the maximum tensile strain, and (iii) 0–300 stands for creep-fatigue test with the creep dwells applied at the maximum compressive strain.

2.3. Microstructure evaluation techniques

Prior to the mechanical tests, three cubic shaped specimens (8 mm × 8 mm × 8 mm) were extracted from the characteristic locations (outermost, middle and innermost) of the forged and precipitation hardened GH4169 superalloy disc, Fig. 1a. These specimens were used to examine the microstructure inhomogeneity by using both optical and scanning electron microscopy (OM and SEM). Specimens were metallographically polished down to 1 μm diamond finish and then etched using the chemical solution that contained 50 ml HCl, 40 ml H_2O, 10 ml HNO_3 and 2.5 g $CuCl_2$ to reveal the microstructure features. Grain size measurements were carried out using the linear intercept method, conforming to ASTM E-112 standard [24]. Hitachi S-4800 SEM was used to examine the distributions of intergranular δ phase of the precipitation hardened GH4169 superalloy specimens. The area fraction of the intergranular δ phase was measured by Image-Pro Plus software on the SEM images with a total scanning area of 600 μm × 400 μm. This method was adopted by Li et al. [25] to quantify the distribution of intergranular δ phase. Micro-hardness measurements were made on each specimen that had been extracted from the outermost, middle and innermost locations of the disc. CamScan Apollo

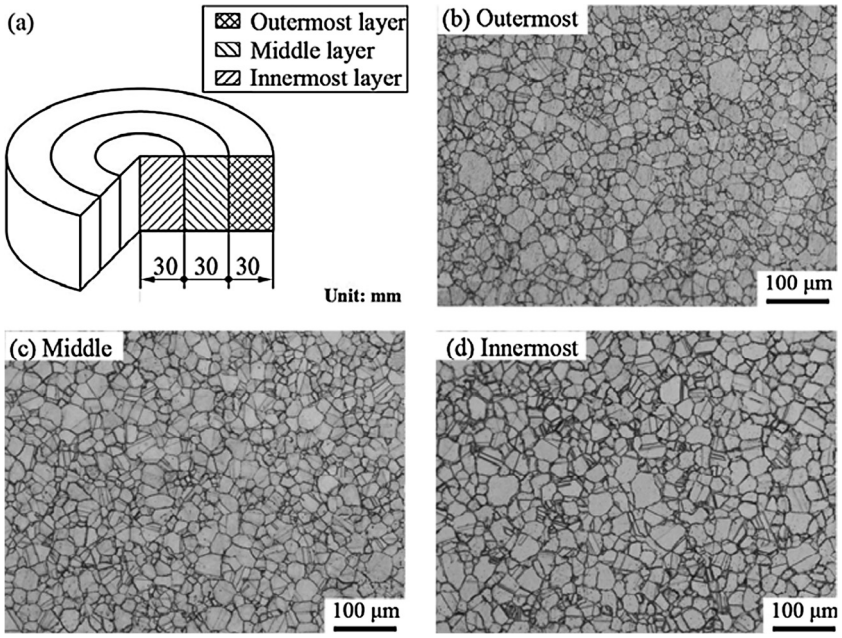

Fig. 1. (a) A schematic diagram of the forged disc with indications of three characteristic locations and (b) to (d) optical micrographs of the forged and precipitation hardened GH4169 superalloy specimens that were extracted from outermost, middle, and innermost locations of the disc, respectively.

Table 1
Chemical composition (wt.%) of GH4169 superalloy.

C	Mn	Fe	S	P	Cr	Mo	Nb	Ti	Al	B	Ni
0.034	0.04	18.50	0.001	0.008	18.91	3.00	5.01	0.99	0.52	0.003	Bal.

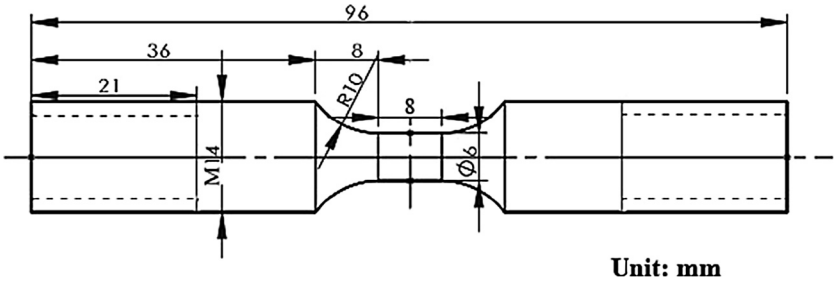

Fig. 2. Dimensions of the uniaxial round bar specimen for both the HTLCF and creep-fatigue tests.

Table 2
Summary of test specimens for the HTLCF and creep-fatigue experiments.

HTLCF tests			Creep-fatigue tests				
ID	Location	$\Delta\varepsilon_t$ (%)	ID	Location	$\Delta\varepsilon_t$ (%)	t_d (s)	t_e (s)
F-1[b]	Outermost	1.0	CF-1[b]	Outermost	1.0	300	0
F-2[b]	Outermost	1.2	CF-2[b]	Outermost	1.0	0	300
F-3[b]	Outermost	1.6	CF-3[b]	Outermost	1.2	300	0
F-4[a,b]	Outermost	2.0	CF-4[b]	Outermost	1.2	0	300
F-5	Middle	1.0	CF-5[b]	Outermost	1.6	300	0
F-6	Middle	1.2	CF-6[b]	Outermost	1.6	0	300
F-7	Middle	1.6	CF-7[a,b]	Outermost	2.0	300	0
F-8	Middle	2.0	CF-8[a,b]	Outermost	2.0	0	300
F-9	Innermost	1.0	CF-9	Middle	2.0	300	0
F-10	Innermost	2.0	CF-10	Middle	2.0	0	300
			CF-11	Innermost	2.0	300	0
			CF-12	Innermost	2.0	0	300

[a] Fractography used to represent the other specimens.
[b] Secondary cracks.

300 SEM equipped with an electron backscatter diffraction (EBSD) detector was used to examine grain-to-grain misorientation with a particular emphasis on the frequencies of Σ3 CSL boundaries. Since EBSD is a surface-sensitive technique, the metallographically polished specimen (down to 0.04 μm diamond finish) was subjected to an additional polishing stage using colloidal silica OPS suspension. This specimen preparation procedure is critical to achieve a good EBSD data, as described in [26]. The EBSD scans were done with a step size of 0.5 μm and the collected data were analysed by using Oxford Instruments HKL Channel 5. Different types of CSL boundaries were identified according to the Brandon criterion by using the post-processing Tango software [27].

Fractography examination by SEM was carried out on selected post-test specimens to identify the high temperature failure mode, as schematically illustrated in Fig 3. Specimens F-4 (0–0), CF-7 (300–0) and CF-8 (0–300) were selected to investigate the effect of creep dwells on material failure mode. They were extracted from the outermost location of the disc and then tested at $\Delta\varepsilon_t = 2.0\%$, Table 2. In addition, selected post-test specimens were sectioned along the longitudinal direction (loading direction) and then examined by OM and SEM micrographs to investigate secondary cracks primarily and microstructure changes, as schematically illustrated in Fig. 3. These included specimens F-1 to F-4 as well as CF-1 to CF-8 at the outermost location with $\Delta\varepsilon_t$ ranging from 1.0% to 2.0%, see Table 2.

3. Results

3.1. Forged and heat treated microstructures

Typical microstructures of the heat treated GH4169 superalloy specimens are shown in Fig. 1b–d for outermost, middle and innermost locations of the disc, respectively. A higher number of twinning boundaries can be observed in Fig. 1d for the innermost location, when compared with those for the outermost (Fig. 1b) and middle locations (Fig. 1c). The average grain size for the innermost location was measured to be 24.7 ± 1.9 μm, compared with that of 20.1 ± 1.1 μm for the middle location, and that of 15.6 ± 1.4 μm for the outermost location, Table 3. In addition, the innermost location had the smallest micro-hardness value of 507.4 ± 29.5 among the three, Table 3. The area fraction of intergranular δ phase for each location is also given in Table 3, where the innermost location had the lowest value of 2.1% among the three. A SEM micrograph for the innermost location of the disc is shown in Fig. 4, where the precipitation of intergranular δ phase can be seen. The presence of intergranular δ phase on precipitation hardened nickel-based superalloys following the heat treatment in this paper have been reported previously for both GH4169 superalloy [25] and Inconel 718 [19].

The frequency distributions of low Σ-value boundaries, namely CSL boundaries for the outermost, middle and innermost locations of the disc are shown in Fig. 5a. It is clear that the Σ3 CSL boundaries are the highest among the other Σ-value boundaries (9.5%, 14.0% and 30.2% of all high angle boundaries for the outermost, middle and innermost locations, respectively). These values are also summarised in Table 3. The EBSD orientation maps in Fig. 5b–d illustrate distributions of Σ3 CSL boundaries (red lines represent Σ3 CSL boundaries). It also confirms that the majority of the CSL boundaries in three locations (outermost, middle and innermost) are Σ3 CSL boundaries. The second highest low Σ-value boundaries at three locations are Σ9 CSL boundaries, Fig. 5a.

3.2. HTLCF testing

The hysteresis loops at half-life cycle of specimens F-1 to F-4 (outermost, 0–0) with $\Delta\varepsilon_t$ ranging from 1.0% to 2.0% are shown in Fig. 6a. The magnitudes of both cyclic stress range at half-life, $\Delta\sigma$, and cyclic plastic range at half-life, $\Delta\varepsilon_p$, increased with the increase in $\Delta\varepsilon_t$, as schematically shown in Fig. 6a for specimen F-4 (0–0). The hysteresis loops at half-life cycle of specimens F-4 (outermost, 0–0), F-8 (middle, 0–0) and F-10 (innermost, 0–0) at $\Delta\varepsilon_t = 2.0\%$ are shown in Fig. 6b. Specimen F-10 (innermost, 0–0) shows the smallest $\Delta\sigma$ and $\Delta\varepsilon_p$ among the three specimens, Fig. 6b. The relationship between cyclic stress amplitude, $\Delta\sigma/2$, and cyclic plastic strain amplitude at half-life, $\Delta\varepsilon_p/2$, can be presented as the following relationship according to [23], i.e.,

$$\frac{\Delta\sigma}{2} = K'\left(\frac{\Delta\varepsilon_p}{2}\right)^{n'} \quad (1)$$

where K′ is the cyclic strength coefficient in MPa and n′ is the cyclic strength exponent. Fig. 7 presents all the experimental data in terms of $\Delta\sigma/2$ and $\Delta\varepsilon_p/2$ at half-life cycle of specimens F-1 to F-10. The relationship given in Eq. (1) was used to provide the best fit to these collated data in Fig. 7; K' = 1013.44 MPa and n' = 0.082 were obtained. In general, the innermost location had the smallest values of $\Delta\sigma/2$ and $\Delta\varepsilon_p/2$, then the middle location and finally the outermost location, Fig. 7. However, it should be noted that specimens F-1 (outermost, 0–0), F-5 (middle, 0–0) and F-9 (innermost, 0–0), all tested at $\Delta\varepsilon_t = 1.0\%$, did not show a significant location-dependence, see the black circle in Fig. 7. This could be attributed to the smallest value of $\Delta\varepsilon_p$ for these tests. It is also noteworthy that specimen F-6 (middle, 0–0) with $\Delta\varepsilon_t = 1.2\%$ had much

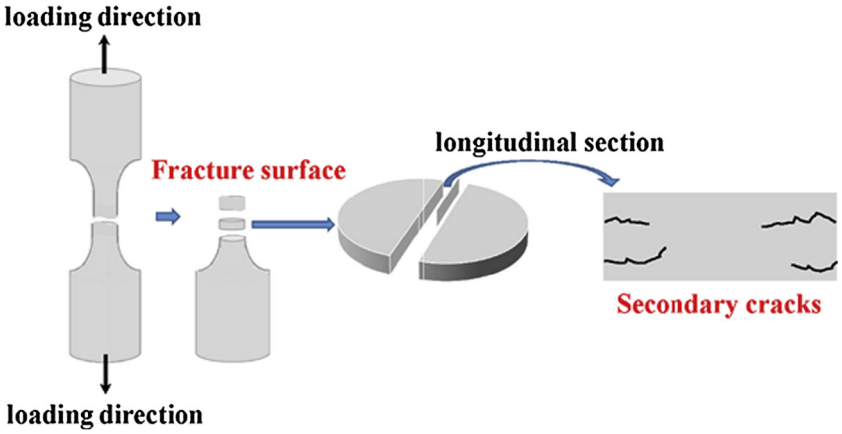

Fig. 3. Schematic diagrams illustrating the specific location of the specimen for carrying out the post-test examination.

Table 3
Summary of microstructure characterization results on GH4169 superalloy.

Location	Grain size (μm)	Micro-hardness (HV)	Area fraction of δ phase (%)	Frequency of Σ3 Boundary (%)
Innermost	24.7 ± 1.9	507.4 ± 29.5	2.1	30.2
Middle	20.1 ± 1.1	542.7 ± 18.0	3.8	14.0
Outermost	15.6 ± 1.4	546.3 ± 21.1	4.1	9.5

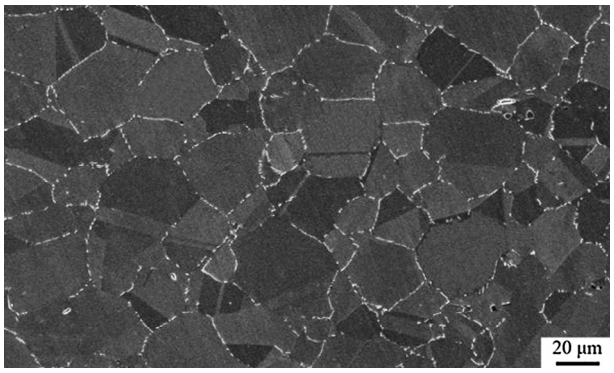

Fig. 4. A representative SEM micrograph of the forged and precipitation hardened GH4169 superalloy that had been extracted from the innermost location of the disc, showing the presence of intergranular δ phase

smaller $\Delta\sigma/2$ and $\Delta\varepsilon_p/2$ than the prediction, see Fig. 7. This may be because the special sampling location for specimen F-6 cannot completely conform to the microstructural regularity of the disc mentioned in Section 3.1. The numbers of cycles to failure, N_f, for specimens F-1 to F-10 are shown in Fig. 8, where innermost location had the highest N_f, which was followed by the middle location and the outermost location had the lowest N_f. The only exception from this trend was the tests carried out at $\Delta\varepsilon_t = 1.6\%$, where the outermost location had a slightly higher N_f than that of the middle location.

3.3. Creep-fatigue testing

Fig. 9a shows the hysteresis loops at half-life of creep-fatigue specimens CF-7 (outermost, 300–0) and CF-8 (outermost, 0–300) as well as HTLCF specimen F-4 (outermost, 0–0). The presence of stress relaxation can be seen in specimen CF-7 at the maximum tensile strain and specimen CF-8 at the maximum compressive strain. Stress relaxation occurred by converting the elastic strain to creep strain during the period of creep dwell. For specimen CF-7 (outermost, 300–0) in Fig. 9a, the inelastic strain range, $\Delta\varepsilon_{in}$, can be calculated by the summation of plastic strain, $\Delta\varepsilon_{pp}$, and the additional tensile creep strain, $\Delta\varepsilon_{cp}$. The value of $\Delta\varepsilon_{pp}$ was determined from the HTLCF test of specimen F-4, and the value of $\Delta\varepsilon_{cp}$ was determined from the tensile stress relaxation period of specimen CF-7, Fig. 9a. Similarly, the inelastic strain range $\Delta\varepsilon_{in}$ for specimen CF-8 (outermost, 0–300) can be calculated by the summation of $\Delta\varepsilon_{pp}$ and $\Delta\varepsilon_{pc}$, Fig. 9a.

The hysteresis loops at half-life cycle of specimens CF-7 (outermost, 300–0), CF-9 (middle, 300–0) and CF-11 (innermost, 300–0) with $\Delta\varepsilon_t = 2.0\%$ are shown in Fig. 9b. Specimen CF-11 (innermost, 300–0) had the smallest values of $\Delta\varepsilon_{in}$ and $\Delta\sigma$, while specimen CF-7 (outermost, 300–0) had the largest values of $\Delta\varepsilon_{in}$ and $\Delta\sigma$, Fig. 9b. The hysteresis loops at half-life cycle of specimens CF-8 (outermost, 0–300), CF-10 (middle, 0–300) and CF-12 (innermost, 0–300) with $\Delta\varepsilon_t = 2.0\%$ are shown in Fig. 9c. Specimen CF-12 (innermost, 0–300) had the smallest values of $\Delta\varepsilon_{in}$ and $\Delta\sigma$, while specimen CF-8 (outermost, 0–300) had the largest values of $\Delta\varepsilon_{in}$ and $\Delta\sigma$, see Fig. 9c. In summary, for both the (300–0) and

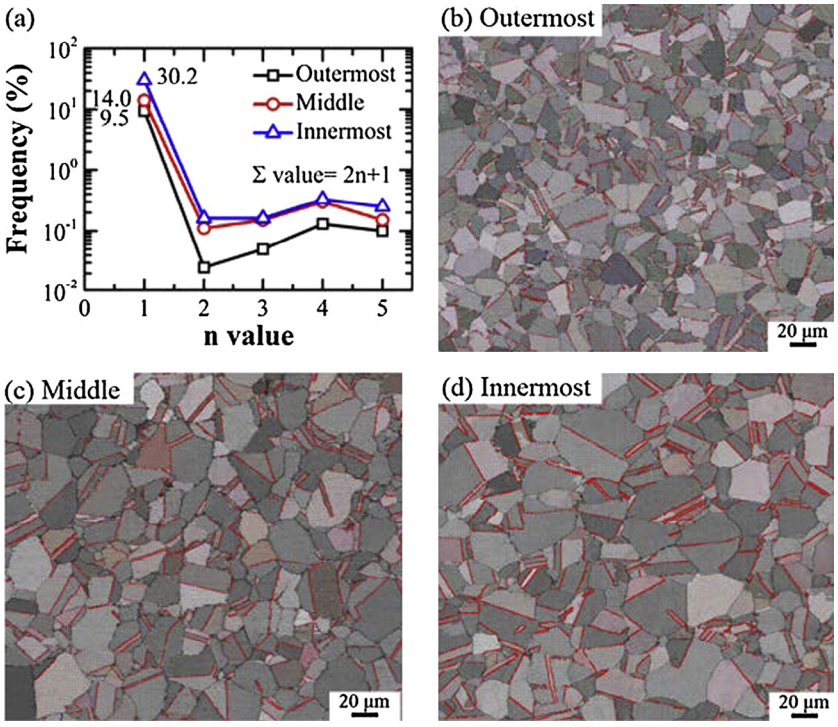

Fig. 5. (a) The frequency of five CSL twin boundaries (Σ3, Σ5, Σ7, Σ9 and Σ11) at three locations of the disc, and (b) to (d) showing distributions of Σ3 twin boundaries at outermost, middle, and innermost locations, respectively. Note: red lines in (b) to (d) represent Σ3 twin boundaries.

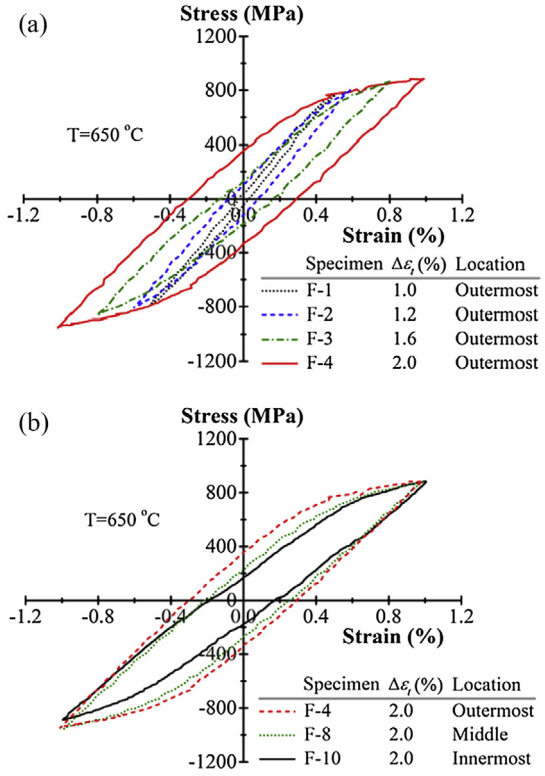

Fig. 6. (a) The hysteresis loops at half-life cycle in HTLCF tests at the outermost location with $\Delta\varepsilon_t$ of 1.0%, 1.2%, 1.6% and 2.0% (specimens F-1 to F-4), and (b) the hysteresis loops at half-life cycle in HTLCF tests with $\Delta\varepsilon_t$ of 2.0% for specimens F-4 (outermost), F-8 (middle) and F-10 (innermost).

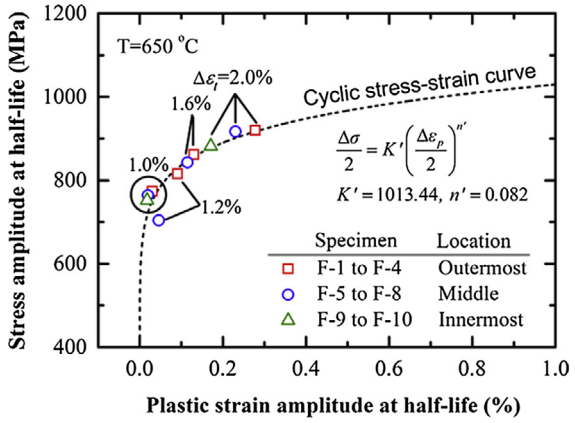

Fig. 7. Experimental data of stress amplitude and plastic strain amplitude at half-life cycle for all HTLCF tests (specimens F-1 to F-10) as well as the cyclic stress-strain curve produced by the best fit to those experimental data.

(0–300) types creep-fatigue tests, the innermost location GH4169 material always had the smallest values of $\Delta\varepsilon_{in}$ and $\Delta\sigma$ among the three locations.

The numbers of cycles to failure of specimens CF-1 to CF-8 are shown in Fig. 10a. These specimens were all extracted from the outermost location and then tested with a range of $\Delta\varepsilon_t$ from 1.0% to 2.0%, Table 2. In general, the numbers of cycles to failure for creep-fatigue tests with creep dwells at the maximum tensile strain (300–0) were slightly lower than those for creep-fatigue tests with creep dwells at the maximum compressive strain (0–300). The numbers of cycles to failure for specimens CF-7 to CF-12 that were all tested at $\Delta\varepsilon_t = 2.0\%$ are shown in Fig. 10b.

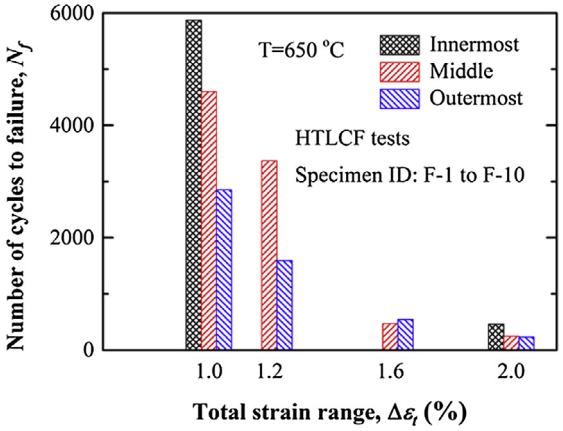

Fig. 8. The numbers of cycles-to-failure in HTLCF tests at three different locations with $\Delta\varepsilon_t$ of 1.0%, 1.2%, 1.6% and 2.0% (specimens F-1 to F-10).

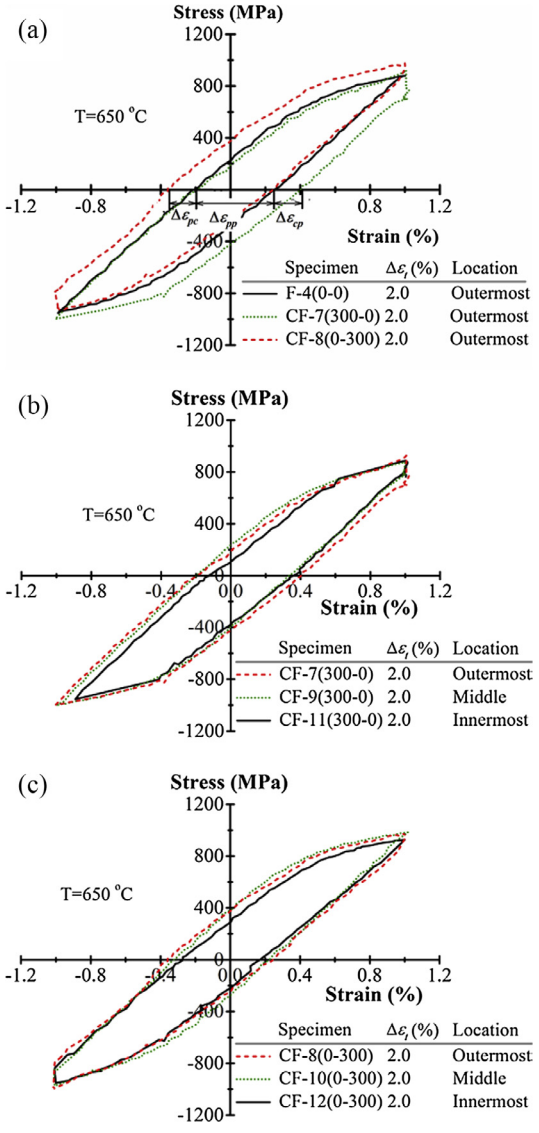

Fig. 9. (a) The hysteresis loops at half-life cycle in HTLCF and creep-fatigue tests of specimens F-4 (outermost, 0–0), CF-7 (outermost, 300–0) and CF-8 (outermost, 0–300); (b) the hysteresis loops at half-life cycle in creep-fatigue tests of specimens CF-7 (outermost, 300–0), CF-9 (middle, 300–0) and CF-11 (innermost, 300–0); (c) creep-fatigue tests of specimens CF-8 (outermost, 0–300), CF-10 (middle, 0–300) and CF-12 (innermost, 0–300).

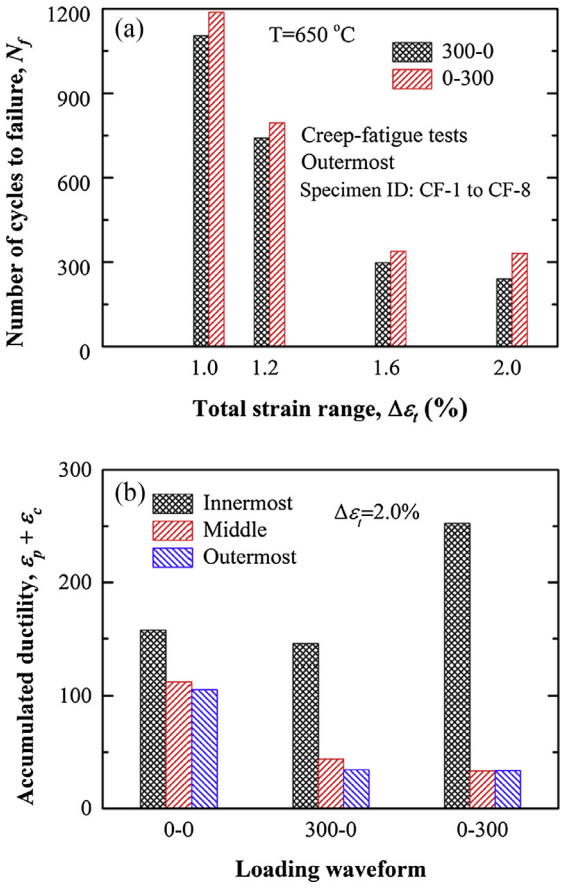

Fig. 10. (a) The numbers of cycles to failure in creep-fatigue tests of specimens CF-1 to CF-8 for a range of $\Delta\varepsilon_t$, and (b) the numbers of cycles to failure in creep-fatigue tests of specimens CF-7 to CF-12. Note: Creep-fatigue tested with creep dwells at the maximum tensile strain is abbreviated as 300–0, and those with creep dwells at the maximum compressive strain is abbreviated as 0–300.

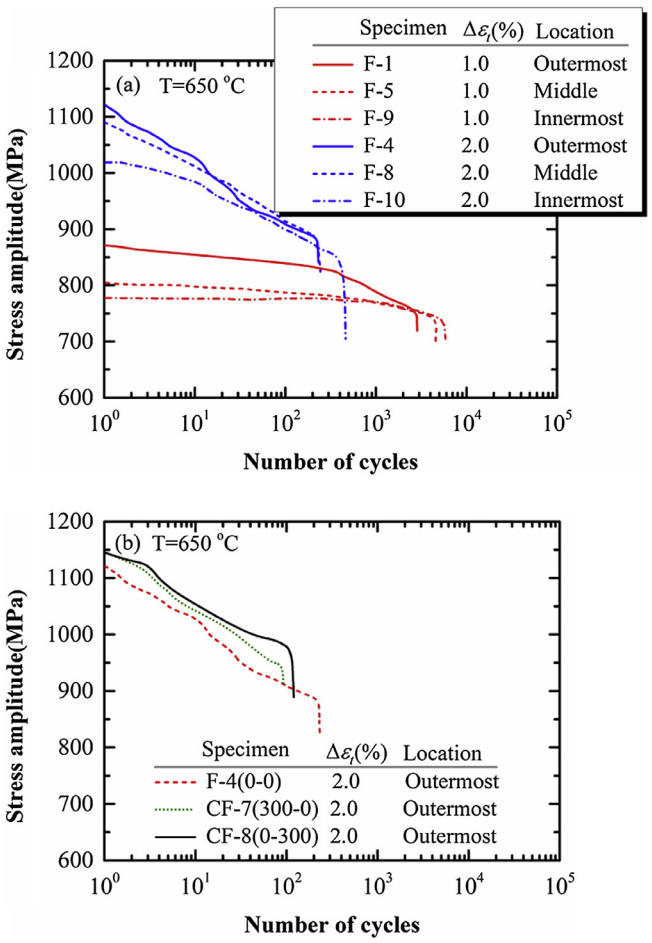

Fig. 11. The cyclic stress response (CSR) curves: (a) HTLCF tests at different locations with $\Delta\varepsilon_t$ of 1.0% (specimens F-1, F-5 and F-9) and 2.0% (specimens F-4 F-8 and F-10); (b) creep-fatigue tests at the outermost location under different loading waveforms with $\Delta\varepsilon_t$ of 2.0% (specimens F-4, CF-7 and CF-8).

Specimen CF-11 (innermost, 300–0) and specimen CF-12 (innermost, 0–300) had the highest number of cycles to failure, while specimen CF-7 (outermost, 300–0) and specimen CF-8 (outermost, 0–300) had the lowest number of cycles to failure, Fig. 10b.

3.4. Cyclic stress response behaviours

The cyclic stress responses (CSRs) of selected specimens are shown in Fig. 11a and b, where the stress amplitude was plotted against the number of cycles. The CSR curves of specimens F-1 (outermost), F-5 (middle), F-9 (innermost) that were tested at $\Delta\varepsilon_t = 1.0\%$ as well as specimens F-4 (outermost), F-8 (middle), F-10 (innermost) that were tested at $\Delta\varepsilon_t = 2.0\%$ are shown in Fig. 11a. The presence of continuous cyclic softening behaviour can be seen for all specimens, indicating that this is a common phenomenon for GH4169 superalloy. In addition, the magnitude of stress amplitude decreased gradually for the majority of fatigue cycles, Fig. 11a. Once macrocrack initiation occurred, the magnitude of stress amplitude decreased rapidly, indicating that the presence of accelerated crack growth at the final stage of HTLCF tests. Also shown in Fig. 11a is that the magnitudes of cyclic softening rate in specimens F-4 (outermost), F-8 (middle) and F-10 (innermost) with $\Delta\varepsilon_t = 2.0\%$ are greater than those in specimens F-1 (outermost), F-8 (middle) and F-9 (innermost) with $\Delta\varepsilon_t = 1.0\%$. Furthermore, in terms of the location-dependence, the stress amplitudes and cyclic softening rates for specimens F-1 (outermost) and F-4 (outermost) were the highest, and specimens F-9 (innermost) and F-10 (innermost) were the lowest. The CSR curves of specimens F-4 (outermost, 0–0), CF-7 (outermost, 300–0), and CF-8 (outermost, 0–300) are shown in Fig. 11b, where specimen F-4 (outermost, 0–0) had the smallest stress amplitude.

3.5. Post test examinations

Fig. 12 shows an overall fracture appearance of specimen F-4 (outermost, 0–0) at $\Delta\varepsilon_t = 2.0\%$, where multiple crack initiation sites can be observed. The fracture surface can be divided into three zones: (i) crack initiation, (ii) crack propagation, and (iii) transient fracture, Fig. 12. The overall fracture appearance of specimen F-4, Fig. 12, is typical of those observed in other specimens. Transgranular fracture features dominated in HTCLF tests. Creep-fatigue tests with tensile dwell period had both transgranular and intergranular fracture features. SEM fractography of specimen CF-7 (outermost, 300–0) with $\Delta\varepsilon_t = 2.0\%$ is shown in Fig. 13a and b, where the presences of intergranular fracture facets and secondary cracks at both crack initiation and crack propagation zones can be found. More transgranular fracture features can be observed at the crack initiation zone in creep-fatigue tests with compressive dwell period, by comparison with those with tensile dwell period. SEM fractography of specimen CF-8 (outermost, 0–300) with $\Delta\varepsilon_t = 2.0\%$ is shown in Fig. 13c, where the presences of circumferential striations at the crack initiation zone can be found.

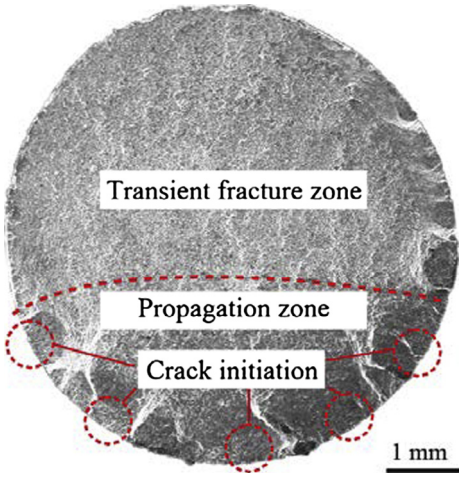

Fig. 12. The overall fracture appearance of specimen F-4, (outermost, 0–0).

The OM micrographs of secondary cracks obtained from specimens CF-7 (300–0) and CF-8 (0–300) are shown in Fig. 14a and b, where both the transgranular and intergranular type crack initiation can be seen. Furthermore, Fig. 15a and b shows the SEM micrographs of the secondary cracks for specimen CF-7 (300–0) and CF-8 (0–300), respectively. In this case, crack lengths of both specimens were greater than 100 μm. Both the intergranular and transgranular features can be seen in Fig. 15a and b. For specimen CF-7 (300–0), several grain boundary damaged areas, i.e. intergranular type damage, can be found, as indicated by A, B and C in Fig. 15a. In contrast, specimen CF-8 (0–300) had thick oxide layer along the crack path until the crack tip region, Fig. 15b. In addition, not significant grain boundary damaged areas can be found in specimen CF-8 (0–300), Fig. 15b. It is also worthwhile to mention that the effect of sampling location on the fracture mode and distribution of secondary cracks was found to be insignificant.

Specimens F-1 to F-4 (outermost, 0–0), specimens CF-1, CF-3, CF-5, CF-7 (outermost, 300–0) as well as specimens CF-2, CF-4, CF-6, CF-8 (outermost, 0–300) with ranging from 1.0% to 2.0% are investigated to describe the quantitative results in terms of secondary cracks. Seldom secondary cracks are visible on the surfaces of the specimens in the HTLCF tests, whereas creep-fatigue specimens present numerous secondary cracks on the surfaces. In addition, more than 40% of the secondary cracks are manifested as intergranular cracking initiation mode for the specimens in creep-fatigue tests. On the contrary, the secondary cracks are almost manifested as transgranular one for those in HTLCF tests. However, in both the HTCLF and creep-fatigue tests, with increasing the magnitudes of $\Delta\varepsilon_t$, the numbers of secondary cracks increase and proportions of intergranular cracking initiation decrease.

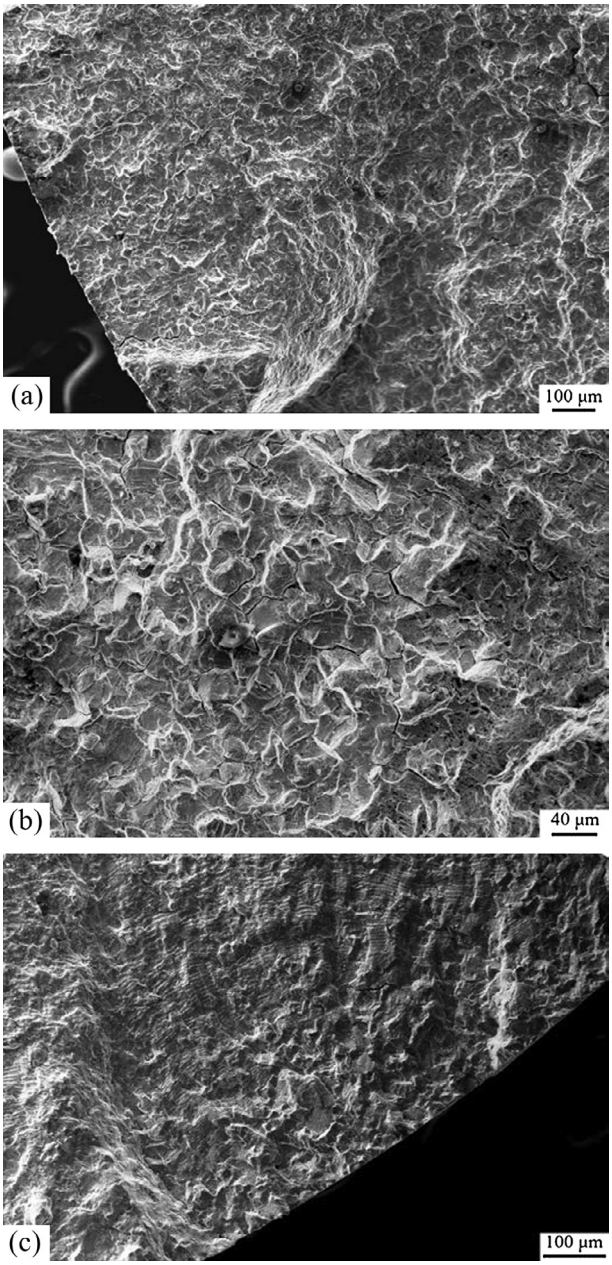

Fig. 13. SEM micrographs of some intergranular fracture surfaces of specimens CF-7 (outermost, 300–0) at the (a) crack initiation zone, and (b) crack propagation zone. (c) SEM micrographs of the presences of circumferential striations of specimens CF-8 at the crack initiation zone (outermost, 0–300).

4. Discussion

4.1. Inhomogeneous microstructure of the disc

The inhomogeneous microstructures among three locations (Table 3) were mainly attributed to high temperature diffusion annealing process. The presence of temperature gradient across different locations of the GH4169 disc during the cooling stage is expected.

Most of the Σ3 CSL boundaries are manifested as the annealing twins (Fig. 5) [28]. The formation of annealing twins is related to the grain boundary migration and the velocity of migration increases with increasing the grain boundary curvature as well as the grain size [29–31]. These observations are consistent with the present experimental work where the length frequencies of Σ3 CSL boundaries increase with the increasing grain sizes for the three disc locations, Table 3.

The relationships between grain size, d, and micro-hardness values at different locations (Table 3) could be described by the Hall-Petch relationship, where the hardness values are proportional to $d^{-1/2}$ [32], Fig. 16. The hardness values increased as the grain sizes decreased for the three locations, Fig. 16. The classic Hall-Petch relationship is based on the consideration that all the random high angle grain boundaries (HAGBs) are obstacles to the dislocation movement [33]. It is known that the CSL boundaries, in particular for Σ3 CSL boundaries, are not effective in resisting penetration by dislocation movement [34]. This is because Σ3 CSL boundaries that represent the misorientation of 60° about a

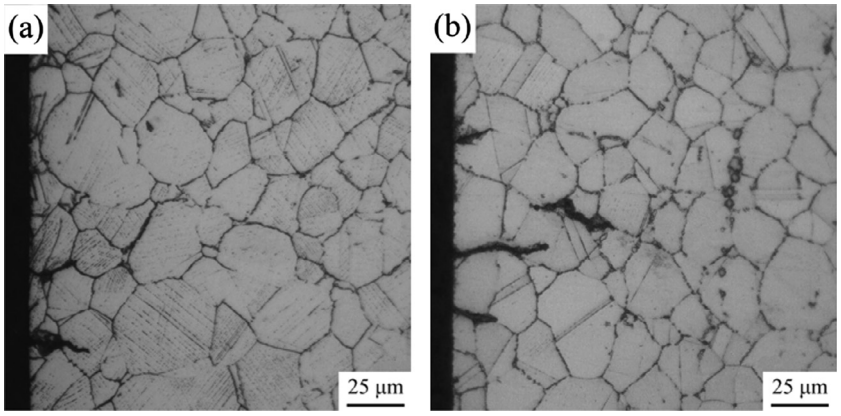

Fig. 14. The OM micrographs of the secondary cracks in the longitudinal section of (a) specimens CF-7 (300–0), (b) and CF-8 (0–300).

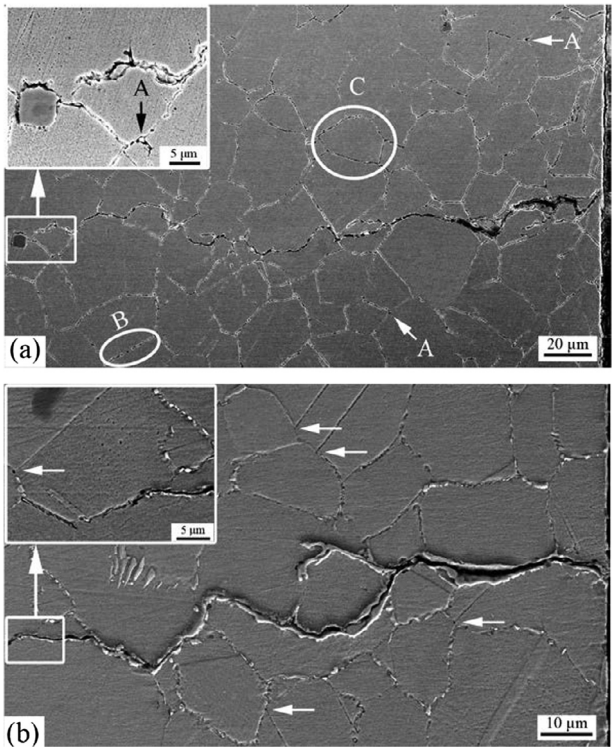

Fig. 15. The SEM micrographs of secondary cracks in creep-fatigue tests of (a) specimen CF-7 (300–0), and (b) CF-8 (0–300). Note: A micro-cracks at triple grain boundary junctions, B coalescence occurring with the surrounding micro-cracks, C linkage between voids and micro-cracks. Arrows in Fig. 15b show the positions of the slip-band-induced micro-cracks.

⟨1 1 1⟩ axis have the coincident site lattice and aligned edges [34,35]. As a consequence, the length frequencies of Σ3 CSL boundaries, *p*, have some impact on Hall-Petch relationship, which could result in some deviations in Fig. 16.

4.2. The effect of microstructural inhomogeneity on HTLCF and creep-fatigue

The accumulated fatigue ductility, ε_p, under a pure fatigue loading test can be calculated based on the relationship given by Edmund and White [36]:

$$\varepsilon_p = \Delta\varepsilon_p \cdot N_f \tag{2}$$

where N_f is the number of cycles to failure for HTLCF tests. The accumulated creep ductility, ε_c, under a creep-fatigue test can be

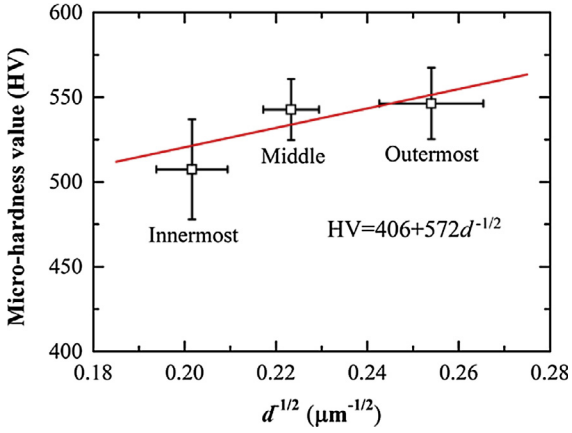

Fig. 16. Hall-Petch relationship to GH4169 superalloy extracted from different locations.

calculated based on the early ductility exhaustion approach used by Priest et al. [37]:

$$\varepsilon_c = \frac{\Delta\varepsilon_{cp}}{\frac{1}{N_f} - \frac{\Delta\varepsilon_{pp}}{\varepsilon_p}} \tag{3a}$$

$$\varepsilon_c = \frac{\Delta\varepsilon_{pc}}{\frac{1}{N_f} - \frac{\Delta\varepsilon_{pp}}{\varepsilon_p}} \tag{3b}$$

where N_f is the number of cycles to failure for the creep-fatigue test at the same selected total strain range for HTLCF test. $\Delta\varepsilon_{pp}$ is the plastic strain, $\Delta\varepsilon_{cp}$ and $\Delta\varepsilon_{pc}$ are the creep strain, as defined in Fig. 9a. Thus Eqs. (3a) and (3b) are used to calculate the accumulated creep ductility for creep-fatigue tests with creep dwells at the maximum tensile strain (300–0) and those at the maximum compressive strain (0–300), respectively.

The accumulated fatigue ductility ε_p for specimens F-4 (outermost), F-8 (middle), F-10 (innermost) in HTLCF tests were calculated using Eq. (2). In such a condition, the values of accumulated ductility, $\varepsilon_p + \varepsilon_c$, equal to those of ε_p. While the values of accumulated ductility, $\varepsilon_p + \varepsilon_c$, for creep-fatigue specimens CF-7 to CF-12 were calculated using both Eq. (2) and Eq. (3). All these tests were carried out at $\Delta\varepsilon_t$ of 2.0% and the calculated total ductility are summarised in Fig. 17. For all three test conditions namely, (0–0), (300–0) and (0–300), the innermost location always had the highest accumulated ductility among the three locations. This location-dependent accumulated ductility could be related to the different length frequencies of Σ3 CSL boundaries for the three disc

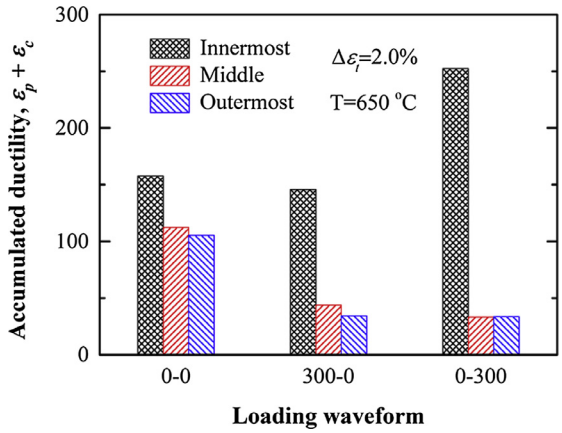

Fig. 17. Summary of accumulated ductility for HTLCF specimens F-4 (outermost), F-8 (middle) and F-10 (innermost) as well as creep-fatigue specimens CF-7 (outermost, 300–0), CF-9 (middle, 300–0), CF-11 (innermost, 300–0), CF-8 (outermost, 0–300), CF-10 (middle, 0–300) and CF-12 (innermost, 0–300).

locations, Table 3. Random HAGBs were regarded as barriers to the dislocation movement from one grain to the adjacent grain because their disordered structures [33,34]. The highest frequency of Σ3 CSL boundaries for the innermost location (Fig. 5a) indicates the lowest frequency of the other types of HAGBs. Thus this accounts for the highest accumulated ductility (both ε_p and ε_c) for the innermost location for (0–0), (300–0) and (0–300) test conditions, Fig. 17. Similarly, the outermost location that had the lowest frequency of Σ3 CSL boundaries (Fig. 5a), namely the highest frequency of the other types of HAGBs, is likely to have more pronounced effects in resisting dislocation motion. Hence the ability to accommodate plastic deformation for the outermost location is manifested by severe loss of ductility, as reported in [34].

During the cyclic deformation process, dislocation recovery occurs and the density of dislocation pile-ups changes with the number of cycles [7]. Dislocation recovery is a thermal-driven process, where the annihilation of dislocations or rearrangement of dislocations occurs. As illustrated in Fig. 11a and b, all the specimens exhibited cyclic softening behaviour over the whole test duration. This is because the selected temperature of 650 °C created a driving force for recovery, as reported for Inconel 718 [38]. Furthermore, the location-dependent CSR behaviours in Fig. 11a could be related to the different dislocation densities. Dislocation sliding is inhibited along the random HAGBs because their incoherent site lattice [34]. Thus, the block of gliding dislocation followed by a stress concentration may be created along the random HAGBs. The internal stress state increases as the pile-up dislocation density increases, leading to a higher macroscopic stress response. As a consequence, the outermost location with highest frequencies of random HAGBs shows the highest stress amplitude for a given strain range among the three, see Fig. 11a. The innermost location gives a more reasonable grain boundary character distribution because Σ3 CSL boundaries could be seemed as a better access to accommodate plastic deformation [35,39]. This may indicate that stabilized cyclic stress response could more easily to be achieved at the innermost location, Fig. 11a.

4.3. Effects of loading waveform and microstructure on high-temperature lifetimes

The presence of different shapes of intergranular δ phase played an important role under tensile strain dwell conditions. Needle-like δ phase in Fig. 18a cause a positive pining effect on the grain boundaries and make grain boundary sliding more difficult for creep tests by Chen et al. [40]. Rod-like δ phase started to separate from the triple grain boundary junctions (position A in Fig. 15a) that can be regarded as a high strain concentration weak position during the drastic cyclic deformation with tensile dwell time. Because of little coherent relation between δ phase and the matrix [25], the precipitate-assist micro-voids will be formed at the junctions [41], as schematically shown in Fig. 18b. After specific cycles, these δ precipitates may separate from the matrix (cycle in Fig. 18a), and then the coalescence occurs with the surrounding micro-cracks, see the position B in Fig. 15b. Finally, the linkage between micro-voids and micro-cracks produces severe intergranular damage, see position C in Fig. 15b.

Creep-fatigue test under compressive strain dwell conditions in Fig. 15b subjected to environmental degradation. In the previous studies focusing on different materials [17,42–44], two possible reasons for life reduction under a compressive dwell period were pointed out. One was the tensile mean stress developing [17,42] and another was the damaging effect of oxidation [42–44]. The former explanation of significant tensile mean stress effect can only be seen at very low strain range and long compressive dwell time for specific materials [17]. Thus, the latter one is concentrated on in this study.

A schematic diagram of cracking initiation and propagation under compressive dwell periods combined with the SEM and EDS observations of short secondary cracks in this study is shown in Fig. 19. A relative thin oxide layer covers the whole material surface and this oxide is mainly suggested to be a protective compact oxide film of Cr_2O_3 [7,13]. After accumulated compressive dwell periods in creep-fatigue tests, the surface oxide grows and the crack may initiates at the most severe defect of the oxide layer [42,43]. Subsequently, the oxide layer spalls during the tension-going direction at a specific cycle [42]. Once the layer is cracked, a fresh matrix is directly in contact with the environment through

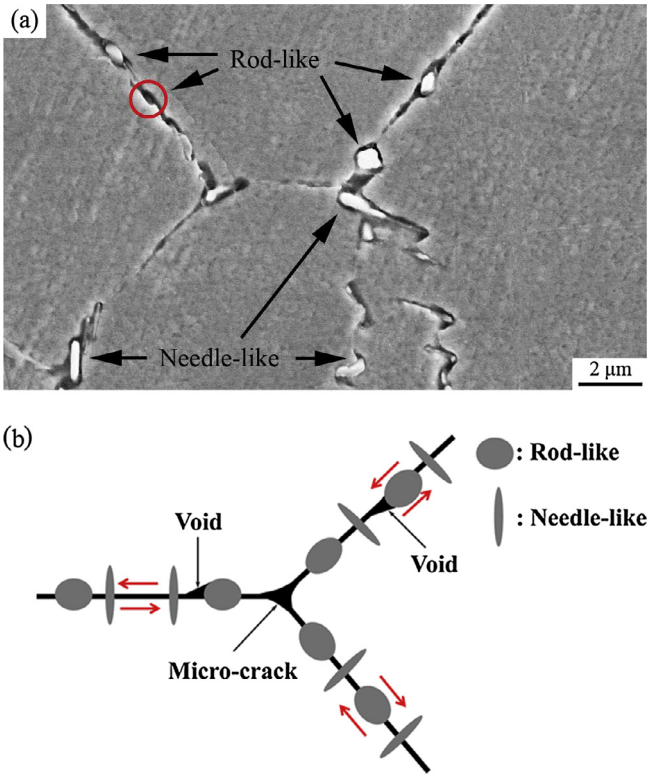

Fig. 18. (a) The formation of precipitate-assist voids in creep-fatigue tests of specimen CF-7 (outermost, 300–0), and (b) corresponding schematic diagram illustrating.

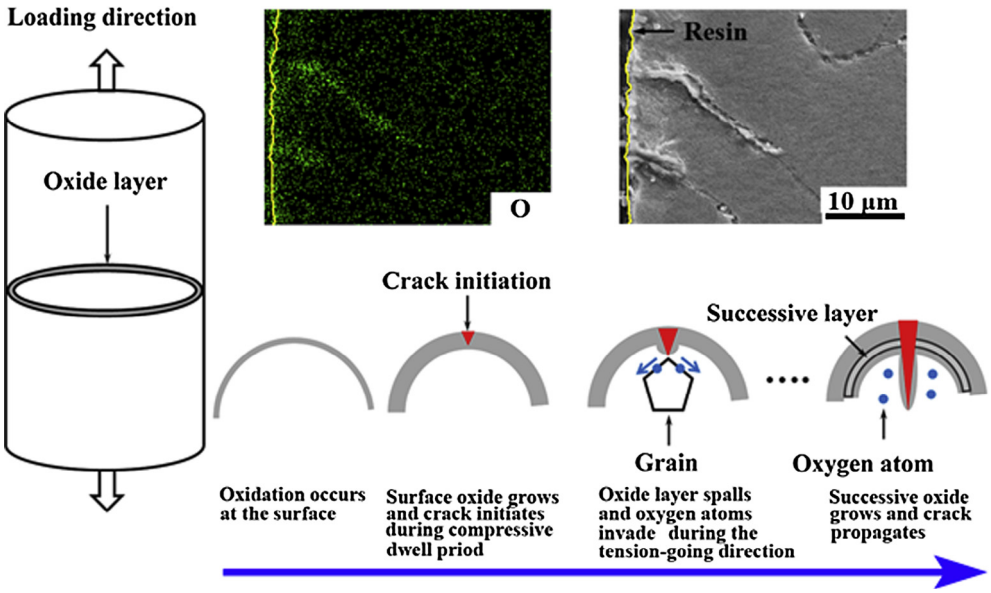

Fig. 19. Suggested mechanism of oxygen penetration and combined SEM and EDS observations of short secondary cracks in creep-fatigue test of specimen CF-8 (outermost, 0–300).

the crack tip, and an internal oxidation zone can be found. After repeating cycles, the above processes repeat resulting in successive oxide layers grow and crack propagates, which can also be observed in the investigation of Andrieu et al. for Inconel 718 [13,44]. As a consequence, the oxidized grain boundary is weakened under compressive dwell period, but no obvious coalescence with micro-cracks under tensile dwell period along the grain boundaries can be seen, Fig. 15b. The following important damage is the introduction of slip-band-induced micro-cracks because the persistent slip bands (PSB) impinge on the brittle oxidized grain boundary to nucleate micro-cracks along the grain boundaries, Fig. 15b.

For nickel-based superalloys, compressive dwells appeared to be more damaging when the small strain range and long dwell time are implied, which was proved by Skelton et al., Takahashi et al. and Brinkman [17,42,43]. However in this study, experimental conditions of relative high $\Delta\varepsilon_t$ and short t_e are out of this range and the tensile dwell period is more damaging than the compressive one, Fig. 10a. Several explanations are given as follows. Firstly, the transition time was investigated to control the progressive process of crack tip oxidation. The environment was viewed as the oxidation-assisted phenomenon before this transition time while that was regarded as the oxidation-dominated phenomenon after this time [13]. In this study, $t_e = 300$ s in one cycle is relative short and the oxidation effect cannot dominant the creep-fatigue lifetimes. Secondly, Fournier et al. [44,45] found that a quite different initiation mechanism by the oxygen penetration at relative low $\Delta\varepsilon_t$. Thirdly, the high values of tensile mean stress were considered to have great impact on lifetimes by the effect on crack closure-opening behaviour during the crack propagation [17,43].

Important special performances on Σ3 CSL boundaries are their lower total interfacial energy, slighter segregation of strengthen alloying elements and lower migration rate followed by lower intergranular precipitation [28,34,35]. Thus, the highest frequencies of Σ3 CSL boundaries at the innermost location are considered as the main explanation for highest HTLCF and creep-fatigue lifetimes. On the one hand, since very low δ phase precipitates and low grain boundary sliding occurs along the Σ3 CSL boundaries, the lowest probability of severe intergranular damage (Fig. 18a and b) at the innermost location among the three can be found. On the other hand, owing to the very difficult diffusive penetration of oxygen atoms into the Σ3 CSL boundaries by means of the transportation from the crack tip (Fig. 19) [46], Σ3 boundaries show supreme resistance to intergranular oxidation. As a consequence, crack tip may be strongly blocked when in contact with Σ3 boundaries in propagation stage [35].

From a macroscopic point of view, numbers of cycles to failure at different locations are directly determined by mechanical behaviours (i.e., inelastic strain ranges, stress amplitudes and plastic strain amplitudes at half-life in Figs. 6b, 9b and c). Thus, there is a need to re-visit some classical creep-fatigue life prediction models and use them to normalize the location-dependence of the creep-fatigue lifetime. This will then help us to establish a robust prediction model that addresses the oxidation effect on creep-fatigue lifetime of GH4169 superalloy.

5. Conclusions

High-temperature low-cycle fatigue and creep-fatigue behaviours of forged and precipitation hardened GH4169 superalloy were investigated. The radial forged disc was divided into three locations because inhomogeneous diffusion annealing leading to different microstructures. The following conclusions were drawn from this work:

(1) The innermost location exhibited the longest fatigue and creep-fatigue resistance performance, while the outermost location had the shortest one because different mechanical behaviours at different locations. It is the outer edge of the disc that experiences the more demanding service environment.
(2) In HTLCF tests, GH4169 superalloy exhibited transgranular crack initiation and propagation type. The introduction of dwell time gradually changed the crack initiation and propagation mode from transgranular to intergranular ones.
(3) Intergranular damage was mainly caused by precipitate-assist micro-voids in the creep-fatigue tests under tensile strain dwell conditions. The oxidation-assisted damage followed by slip-band-induced micro-cracks dominated in the creep-fatigue tests under compressive strain dwell conditions.

Acknowledgements

The author would like to acknowledge gratefully for the financial support through National Natural Science Foundations of China (51371082, 51322510) and the 111 project. The author Xian-Cheng Zhang is also grateful for the support by Shanghai Pujiang Program, Young Scholar of the Yangtze River Scholars Program, and Shanghai Technology Innovation Program of SHEITC (CXY-2015-001). The author Bo Chen acknowledges financial supports from the Centre for Manufacturing and Materials Engineering at Coventry University for facilitating the collaboration.

References

[1] Deng G-J, Tu S-T, Zhang X-C, Wang Q-Q, Qin C-H. Grain size effect on the small fatigue crack initiation and growth mechanisms of nickel-based superalloy GH4169. Eng Fract Mech 2015;134:433–50.
[2] Kuo CM, Yang YT, Bor HY, Wei CN, Tai CC. Aging effects on the microstructure and creep behavior of Inconel 718 superalloy. Mater Sci Eng, A 2009;510–511:289–94.
[3] Leo Prakash DG, Walsh MJ, Maclachlan D, Korsunsky AM. Crack growth micro-mechanisms in the IN718 alloy under the combined influence of fatigue, creep and oxidation. Int J Fatigue 2009;31:1966–77.
[4] Wei D-S, Yang X-G. Investigation and modeling of low cycle fatigue behaviors of two Ni-based superalloys under dwell conditions. Int J Press Vessels Pip 2009;86:616–21.
[5] Pineau A. High temperature fatigue: creep–fatigue–oxidation interactions in relation to microstructure. Subcrit Crack Growth Due Fatigue Corros Creep 1981:483–530.
[6] Rodriguez P, Rao KBS. Nucleation and growth of cracks and cavities under creep-fatigue interaction. Prog Mater Sci 1993;37:403–80.
[7] Pineau A, Antolovich SD. High temperature fatigue of nickel-base superalloys – a review with special emphasis on deformation modes and oxidation. Eng Fail Anal 2009;16:2668–97.
[8] Manson SS, Halford GR. Fatigue and durability of metals at high temperatures. ASM International; 2009.
[9] Zhu S-P, Yang Y-J, Huang H-Z, Lv Z, Wang H-K. A unified criterion for fatigue–creep life prediction of high temperature components. Proc Inst Mech Eng, Part G: J Aerospace Eng 2016. 095441001664144.
[10] Louks R, Susmel L. The linear-elastic theory of critical distances to estimate high-cycle fatigue strength of notched metallic materials at elevated temperatures. Fatigue Fract Eng Mater Struct 2015;38:629–40.
[11] Gallo P, Berto F. Influence of surface roughness on high temperature fatigue strength and cracks initiation in 40CrMoV13. 9 notched components. Theoret Appl Fract Mech 2015;80:226–34.
[12] Berto F, Gallo P. Extension of linear elastic strain energy density approach to high temperature fatigue and a synthesis of Cu-Be alloy experimental tests. Eng Solid Mech 2015;3:111–6.
[13] Andrieu E, Molins R, Ghonem H, Pineau A. Intergranular crack tip oxidation mechanism in a nickel-based superalloy. Mater Sci Eng, A 1992;154:21–8.
[14] Ghonem H, Nicholas T, Pineau A. Elevated temperature fatigue crack growth in alloy 718—Part II: Effects of environmental and material variables. Fatigue Fract Eng Mater Struct 1993;16:577–90.
[15] Ainsworth RA. R5 procedures for assessing structural integrity of components under creep and creep–fatigue conditions. Int Mater Rev 2006;51:107–26.
[16] Brinkman CR, Korth GE. Strain fatigue and tensile behavior of Inconel® 718 from room temperature to 650 °C. J Test Eval 1974;2:249–59.
[17] Brinkman CR. High-temperature time-dependent fatigue behaviour of several engineering structural alloys. Int Met Rev 1985;30:235–58.
[18] He L, Zheng Q, Sun X, Guan H, Hu Z, Tieu K, et al. Effect of temperature and strain amplitude on dislocation structure of M963 superalloy during high-temperature low cycle fatigue. Mater Trans 2006;47:67–71.
[19] Prasad K, Sarkar R, Ghosal P, Kumar V. Simultaneous creep–fatigue damage accumulation of forged turbine disc of IN 718 superalloy. Mater Sci Eng, A 2013;572:1–7.
[20] Khaja S, Mehta KK, Veera Babu R, Sri Rama Devi R, Singh AK. Mechanical properties anisotropy of isothermally forged and precipitation hardened Inconel 718 disk. Metall Mater Trans A 2014;46:1140–53.
[21] Zhang X-C, Li H-C, Zeng X, Tu S-T, Zhang C-C, Wang Q-Q. Fatigue behavior and bilinear Coffin-Manson plots of Ni-based GH4169 alloy with different volume fractions of δ phase. Mater Sci Eng, A 2017;682:12–22.
[22] Xiao L, Chaturvedi M, Chen D. Effect of boron on the low-cycle fatigue behavior and deformation structure of INCONEL 718 at 650 °C. Metall Mater Trans A 2004;35:3477–87.
[23] ASME E 2714–13. Standard test method for creep-fatigue testing. American Society of Testing and Materials; 2013.
[24] ASTM E-112. Standard test methods for determining average grain size. ASTM International USA; 2010.
[25] Li HY, Kong YH, Chen GS, Xie LX, Zhu SG, Sheng X. Effect of different processing technologies and heat treatments on the microstructure and creep behavior of GH4169 superalloy. Mater Sci Eng A-Struct Mater Prop Microstruct Process 2013;582:368–73.
[26] Karamched PS, Wilkinson AJ. High resolution electron back-scatter diffraction analysis of thermally and mechanically induced strains near carbide inclusions in a superalloy. Acta Mater 2011;59:263–72.
[27] Brandon DG. The structure of high-angle grain boundaries. Acta Metall 1966;14:1479–84.
[28] Yamaura S, Igarashi Y, Tsurekawa S, Watanabe T. Structure-dependent intergranular oxidation in Ni–Fe polycrystalline alloy. Acta Mater 1999;47:1163–74.
[29] Mahajan S, Pande C, Imam M, Rath B. Formation of annealing twins in fcc crystals. Acta Mater 1997;45:2633–8.
[30] Pande CS, Imam MA, Rath BB. Study of annealing twins in FCC metals and alloys. Metall Trans A 1990;21:2891–6.
[31] Trimby P. Analysis of the crystallographic signature of electron beam welds in Cu: implications for variations in etching characteristics: Svensk kärnbränslehantering (SKB); 2009.
[32] Armstrong RW. Engineering science aspects of the Hall-Petch relation. Acta Mech 2014;225:1013–28.
[33] Park SHC, Sato YS, Kokawa H. Microstructural evolution and its effect on Hall-Petch relationship in friction stir welding of thixomolded Mg alloy AZ91D. J Mater Sci 2003;38:4379–83.
[34] Lu K, Lu L, Suresh S. Strengthening materials by engineering coherent internal boundaries at the nanoscale. Science 2009;324:349–52.
[35] Krupp U. Dynamic embrittlement—time–dependent quasi–brittle intergranular fracture at high temperatures. Int Mater Rev 2005;50:83–97.
[36] Edmunds HG, White DJ. Observations of the effect of creep relaxation on high-strain fatigue. J Mech Eng Sci 1966;8:310–21.
[37] Priest RH, Ellison EG. A combined deformation map-ductility exhaustion approach to creep-fatigue analysis. Mater Sci Eng 1981;49:7–17.
[38] Fournier D, Pineau A. Low cycle fatigue behavior of inconel 718 at 298 K and 823 K. Metall Trans A 1977;8:1095–105.
[39] Randle V. Twinning-related grain boundary engineering. Acta Mater 2004;52:4067–81.
[40] Chen W, Chaturvedi M. Dependence of creep fracture of Inconel 718 on grain boundary precipitates. Acta Mater 1997;45:2735–46.
[41] Ramirez AJ, Lippold JC. High temperature behavior of Ni-base weld metal. Mater Sci Eng, A 2004;380:245–58.
[42] Skelton RP. Creep-fatigue interactions (crack initiation). Compr Struct Integr 2003;5:25–112.
[43] Takahashi Y. Study on creep-fatigue evaluation procedures for high-chromium steels—Part I: Test results and life prediction based on measured stress relaxation. Int J Press Vessels Pip 2008;85:406–22.
[44] Fournier B, Sauzay M, Caes C, Noblecourt M, Mottot M, Bougault A, et al. Creep-fatigue-oxidation interactions in a 9Cr–1Mo martensitic steel. Part II: Effect of compressive holding period on fatigue lifetime. Int J Fatigue 2008;30:663–76.
[45] Fournier B, Sauzay M, Caes C, Noblecourt M, Mottot M, Bougault A, et al. Creep–fatigue–oxidation interactions in a 9Cr–1Mo martensitic steel. Part III: Lifetime prediction. Int J Fatigue 2008;30:1797–812.
[46] Krupp U, Wagenhuber PEG, Kane WM, McMahon CJ. Improving resistance to dynamic embrittlement and intergranular oxidation of nickel based superalloys by grain boundary engineering type processing. Mater Sci Technol 2005;21:1247–54.